36A.0 MICROSTRUCTURAL EVOLUTION IN TITANIUM ALLOYS UNDER ADDITIVE MANUFACTURING CONDITIONS

Student: Alec Saville (Mines)
Faculty: Amy Clarke (Mines)
Industrial Mentor(s): Adam Pilchak (MRL), Jessica Buckner (SNL), and Andrew Kustas (SNL)

This project started in Fall 2018 and was initially supported by the Office of Naval Research. This project is currently supported by the National Science Foundation Graduate Research Fellowships Program (NSF GRFP). Aspects are also supported by the UD DOE Office of Science. The research performed during this project will serve as the basis for a PhD thesis program for Alec Saville.

36A.1 Project Overview and Industrial Relevance

Over the last decade, metallic additive manufacturing (AM) has seen increasing use in the creation of near-net shape, functional and structural components (not safety critical). The primary benefit of AM over traditional processing is the ability to create custom geometries beyond what is possible with traditional manufacturing, and the reduction of waste associated with extensive machining [36A.1-2]. Several challenges exist in effectively employing, qualifying, and certifying AM parts, limiting metallic AM parts to low-risk applications. These include maintaining control of microstructure during the build process via careful selection of build parameters, limiting defects like porosity and cracking, controlling anisotropic loading responses, and limiting detrimental microstructural formations [36A.3-4]. The influence of processing parameters (e.g., scan strategy, power setting, etc.) on microstructure and defect development is not well understood, and remains an active area of research.

This project focuses on evaluating the response of Ti-6Al-4V microstructures to changes in build parameters and processing conditions during AM, while also exploring new avenues for microstructural refinement in emerging titanium alloys designed specifically for AM. Samples of electron beam melted powder bed fusion (EBM-PBF) Ti-6Al-4V produced with varying scan strategies and wire-arc AM (WAAM) Ti-6Al-4V from a large-volume build are being evaluated to elucidate how changes in build parameters within the same build process (e.g., scan strategy), or changes between build processes (EBM-PBF versus WAAM with significantly different length scales and processing conditions), alter microstructure development. Exploration of microstructural refinement during AM builds with other titanium alloys is also planned as part of future work. The insight gained in this project will also be applied to other alloy systems such as Ti-10-2-3 to explore new avenues for greater microstructural control beyond AM and during deformation.

WAAM Ti-6Al-4V specimens for this work were produced at Sandia National Laboratory (SNL) in a large-bowl build geometry using argon shielding gas (**Figure 36A.1**). Future alloys for studying microstructural refinement will be custom ordered or produced on-site as needed.

36A.2 Previous Work

36A.2.1 WAAM Ti-6Al-4V Microstructural Characterization and Initial Orientation Measurements

Initial SEM imaging of the SNL WAAM Ti-6Al-4V demonstrated a typical microstructure for a directed energy deposition (DED) build process. Regions of thin, basketweave α-Ti with limited β-Ti (**Figure 36A.2a**) were observed, along with thicker basketweave α-Ti with increasing quantities of β-Ti (**Figure 36A.2b**). This change in size and phase fraction indicate noticeable changes in local cooling rates from the last excursion into the β-Ti regime. Local regions of small, elongated colonies (**Figure 36A.2c**) with high aspect ratios and large, thin-plate colonies (**Figure 36A.2d**) were also dispersed throughout the build volume with grain boundary α-Ti, indicating regions of considerably slower solid state cooling.

These results are consistent with prior work by Kelly et al., where each layer of wire deposited material creates a tiered microstructure within a previously deposited layer [36A.5]. When a given layer is deposited, the heat from the deposition process propagates into previously deposited layers. Regions of material at the top of the previous layer encounter the greatest thermal excursion at this point, heating into the β-Ti regime and gradually cooling as the deposition process finishes locally. This slow cooling gives rise to the high aspect ratio colony morphologies.

Locations in the middle of a previous layer are subject to intermediate heating and cooling rates, thereby forming coarse basketweave α-Ti. Material towards the bottom of the layer is subject to the fastest cooling rates, and consequently forms the finer acicular α-Ti with reduced β-Ti phase fractions. These morphologies are not perfectly layered through the build height due to changes in local conditions, but the overall reasoning for each morphology holds in this WAAM build.

Regions of large colonies were also found interspersed throughout the build volume and at the build edges (**Figure 36A.3**). The former was attributed to pauses in the build process, likely producing slower cooling rates at the end of operation, and the latter attributed to reduced overlap of the heat source during deposition. This is despite traditional logic claiming heat transfer from the surface produces faster cooling rates.

A large crack was observed ~ 40 mm up the build height in the as-received specimens, spanning almost the entire width of the build geometry (**Figure 36A.4**). Parallel crack formation was also observed throughout the fractured area, with many cracks propagating without direct connection to one another or a clear boundary guiding travel. These unusual features were investigated using SEM, light optical microscopy (LOM), and EBSD to identify the mechanisms for crack formation and propagation, but no clear answer was identified prior to this reporting period.

36A.2.2 Large-Scale EBSD and Neutron Diffraction of WAAM Ti-6Al-4V

Large-scale EBSD of WAAM Ti-6Al-4V was completed to relate specific orientations to microstructural features observed in the previous reporting period. This also enables the reconstruction of the as-solidified β-Ti microstructure and crystallographic texture. Neutron diffraction up the build height in ~ 10 mm intervals was also completed to assess bulk crystallographic texture as a function of build height.

Previous work on EBM-PBF Ti-6Al-4V identified specific α-Ti orientations that correlate to diffusional microstructures and finer as-solidified β-Ti grains [36A.6]. The presence of these orientations in the WAAM Ti-6Al-4V build was explored by neutron diffraction and EBSD to deconvolute whether these orientations originate from finer as-solidified microstructures, or diffusional solid state microstructures.

Neutron diffraction and EBSD scans returned similar α-Ti textures and favored specific planes similar to those reported in EBM-PBF Ti-6Al-4V with martensitic solid state microstructures [36A.6]. The faster cooling rate basketweave microstructure dominated the surveyed areas, and correspondingly had increased textures of the $\{11\bar{2}0\}_{\alpha}$ planes favored in diffusionless solid state microstructures. This was found regardless of the reconstructed parent β-Ti grain size, measuring millimeters to centimeters in scale (**Figure 36A.5** and **Figure 36A.6**). Fiber textures were also seldom found, but the exact mechanism for this had yet to be identified.

Several regions of varying parent β-Ti grain size were observed at locations where colony $\alpha + \beta$ morphologies dominated the microstructure. As seen in **Figure 36A.7**, these colony regions coincided with melt-pool like β-Ti grains and some equiaxed nucleation of β-Ti. This is theorized to originate from build pauses and restarts changing the thermal conditions for the next layer. With higher heat extraction due to a cooler build volume from the build pause, the newly deposited material favored smaller columnar grains or equiaxed solidification where heat extraction was greatest. The aforementioned colony regions are the last layers of build material deposited before the build pause. Due to the long cooling cycle before the next layer was deposited, these colonies can grow to the large sizes observed.

Portions of the material exhibiting colony microstructures and the "weld pool" β-Ti grains also exhibited the most pronounced cracking, including the near complete cracking of the specimen width at about ~ 40 mm in build height. Such cracking was theorized to originate from residual stresses in the build process aligned parallel to the build direction. The favorable crack propagation in colony microstructures was due to the colonies acting as continuous crystallographic highways, rather than the more tortuous path associated with basketweave microstructures elsewhere in the build. A Schmid factor analysis (**Figure 36A.8**) was completed to prove the crack propagation path through the colony microstructure according to literature findings [36A.7]. It is recommended to avoid build pauses in WAAM Ti-6Al-4V builds to avoid the formation of discontinuous solid state microstructures and consequently reduce cracking formation.

36A.3 Recent Work

36A.3.1 Validating WAAM Ti-6Al-4V Texture and Microstructure Relationships

A systematic analysis of transformation mechanisms was completed in order to connect the texture markers found in previous EBM-PBF Ti-6Al-4V to those found in WAAM Ti-6Al-4V. Large parent β-Ti grains were apparent in both neutron diffraction and EBSD and did not produce significant fiber textures around the solidification direction. The mechanism for this was unknown, but the presence of a fiber texture demonstrated finer β-Ti grain sizes after solidification [36A.6] and was investigated further during this reporting period.

During solidification, β-Ti solidifies with one set of $\{001\}_\beta$ planes parallel to the thermal gradient. This is often close, if not parallel, to the build direction. Following the cubic symmetry of β-Ti, the four remaining $\{001\}_\beta$ planes are free to rotate around the solidification direction. For a single β-Ti grain constituting a part like in **Figure 36A.6**, this results in localized $\{110\}_\beta$ planes and only 12 different orientations for α-Ti to take on in 3D space. No fiber texture is possible (**Figure 36A.9**). However, if several β-Ti grains are present and align along the solidification direction, different orientations are produced. Though all the β-Ti grains will try to align two $\{001\}_\beta$ planes along the solidification direction, the remaining four are free to rotate around the pinned planes. Assuming a random rotation of these four remaining $\{001\}_\beta$ planes, this creates a ring of $\{110\}_\beta$ orientations around the build direction. Following the Burgers orientation relationship (OR), this produces a fiber texture around the solidification direction in the product α-Ti (**Figure 36A.10**). Thus, with more β-Ti grains in the same volume comes a greater chance of free rotation around the solidification direction and the presence of a fiber texture.

Though **Figure 36A.9** and **Figure 36A.10** explain how fiber textures emerge in AM Ti-6Al-4V as a function of β-Ti grain size, the specific α-Ti fiber which forms is not well explained. One fiber texture forming *only* off $\{110\}_\beta$ planes 45° off the solidification direction was favored in diffusional solid state microstructures, while the other formed off $\{110\}_\beta$ planes 90° is favored by diffusionless solid state microstructures. Whether the plane multiplicity or transformation mechanisms regulates the formation of these orientations is unknown and the subject of future work. These results and those of previous reporting periods are planned for publication in *Additive Manufacturing*.

36A.3.2 Reconstruction of Ti-10-2-3

Given that considerable amounts of EBSD data and parent phase reconstructions have been performed to date, a new collaborative effort with postdoc Ben Ellyson was started on the metastable β-Ti alloy Ti-10-2-3. This titanium alloy is known for exhibiting transformation induced plasticity (TRIP), where the metastable β-Ti phase transforms into orthorhombic α'' martensite upon loading and achieves desirable mechanical properties and work hardening rates under high strain rate conditions [36A.8]. This work focuses on reconstructing the parent β-Ti microstructures of lightly deformed specimens to track how the orientation of parent β-Ti grains influences TRIP behavior and consequently mechanical properties at different strain rates.

Test reconstruction of low deformation microstructures was completed on one Ti-10-2-3 sample directly after quenching from the β-Ti regime. The old orientation relationship (OR) for $\beta \rightarrow \alpha''$ [36A.8] and a calculated OR using the reconstruction algorithms in the MATLAB plugin MTEX were implemented to test reconstruction effectiveness. The two OR's both successfully created reconstructed microstrucutres, but the MTEX calculated OR was much more accurate (**Figure 36A.11**). It's unknown specifically why the literature OR incorrectly reconstructed many parent β-Ti grains, but this is the subject of future investigations. Regardless, this process demonstrated it is indeed possible to reconstruct the parent β-Ti grains from partially transformed microstructures, which is being explored for fully transformed microstructures following this technique's validation.

The insight gained here is planned for further work on Ti-10-2-3 in general, where unique stress conditions can create complicated microstructures and ambiguous parent grains (**Figure 36.A.12**). Reconstruction of parent grain microstructures with the process developed here will likely prove useful for enabling more control over microstructural evolution in titanium alloys beyond Ti-6Al-4V.

36A.4 Plans for Next Reporting Period

Future work will focus on publishing results regarding the WAAM Ti-6Al-4V microstructure, texture, and crack propagation and evaluating other titanium alloys for AM applications. Collaborative work with VTT-Finland on phase field modelling of EBM-PBF solidification/solid state transformations and crystal plasticity of the as-built microstructures with deformation is ongoing. Mechanical testing of EBM-PBF Ti-6Al-4V to calibrate these models is planned in the next reporting period, along with publication of Ti-10-2-3 reconstruction efforts and further exploration of this alloy in the context of AM.

36A.5 References

[36A.1] B. Dutta, F.H. (Sam) Froes, The Additive Manufacturing (AM) of titanium alloys, Metal Powder Report. 72 (2017) 96–106.

[36A.2] W. Frazier, Metal Additive Manufacturing: A Review, (2014).

[36A.3] S.S. Al-Bermani, M.L. Blackmore, W. Zhang, I. Todd, The Origin of Microstructural Diversity, Texture, and Mechanical Properties in Electron Beam Melted Ti-6Al-4V, Metallurgical and Materials Transactions A. 41 (2010) 3422–3434.

[36A.4] C.A. Brice, W.A. Tayon, A.L. Pilchak, Texture Development in Titanium Components Made by Additive Manufacturing, San Diego. (2014) 16.

[36A.5] Kelly, S.M., Kampe, S.L., 2004. Microstructural evolution in laser-deposited multilayer Ti-6Al-4V builds: Part I. Microstructural characterization. Metall and Mat Trans A 35, 1861–1867.

[36A.6] Saville, A.I., Vogel, S.C., Creuziger, A., Benzing, J.T., Pilchak, A.L., Nandwana, P., Klemm-Toole, J., Clarke, K.D., Semiatin, S.L., Clarke, A.J., 2021. Texture evolution as a function of scan strategy and build height in electron beam melted Ti-6Al-4V. Additive Manufacturing 46, 102118.

[36A.7] Xie, Y., Gong, M., Luo, Z., Li, Q., Gao, M., Wang, F., Zeng, X., Wang, G., 2021. Effect of microstructure on short fatigue crack growth of wire arc additive manufactured Ti-6Al-4V. Materials Characterization 177, 111183.

[36A.8] Duerig, T.W., Middleton, R.M., Terlinde, G.T., Williams, J.C., 1980. Stress Assisted Transformation In Ti-10V-2Fe-3Al. Titanium ‘80 Science & Technology - Proceedings of the 4th Int’l Conference on Titanium 2.

36A.6 Figures and Tables

Figure 36A.1: Full build volume WAAM Ti-6Al-4V samples were extracted from for characterization (courtesy of SNL). Samples were extracted from the two cut out sections via wire EDM.

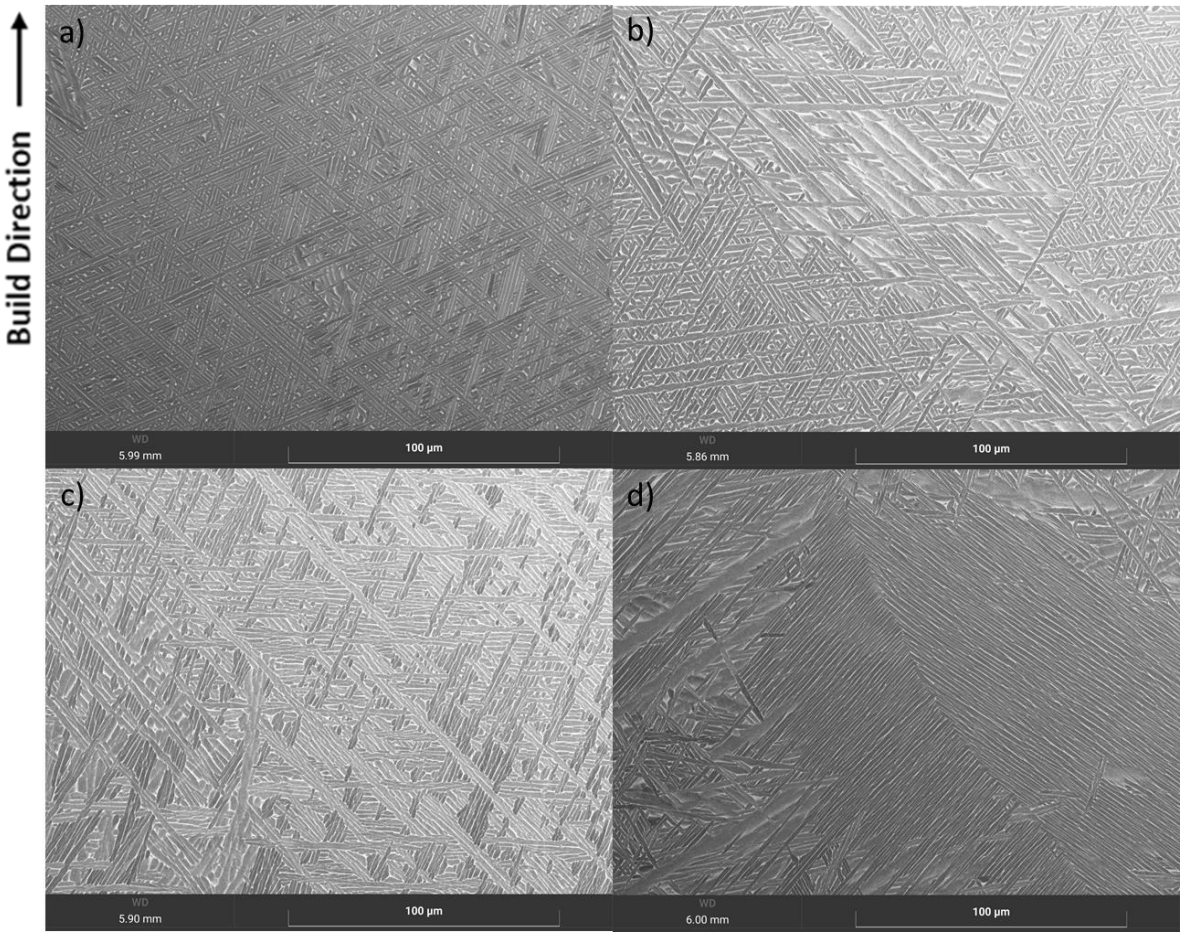

Figure 36A.2: Backscatter electron scanning electron images of the WAAM Ti-6Al-4V build, depicting fine basketweave (a), coarser basketweave (b), small elongated colonies (c), and large thin plate colonies (d).

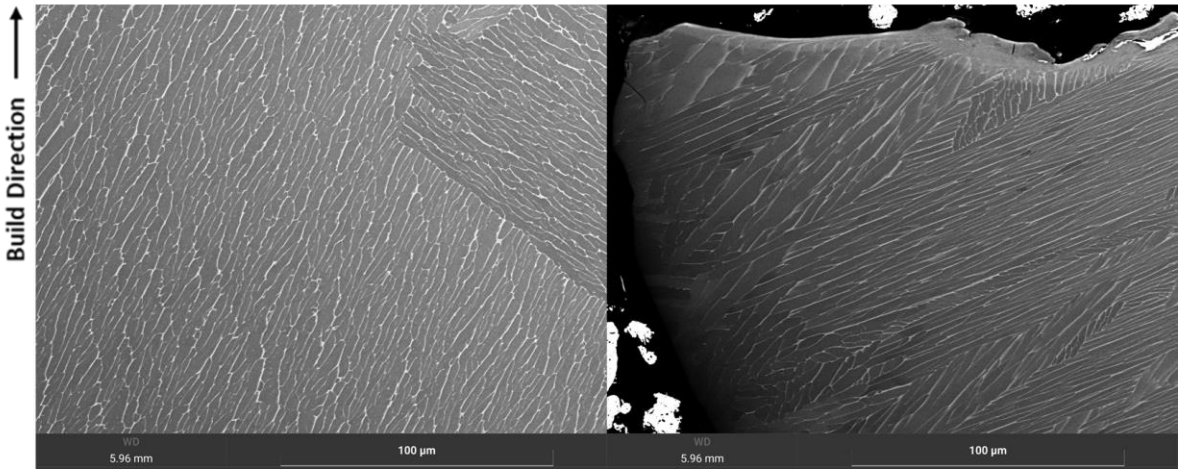

Figure 36A.3: Backscatter electron scanning electron images of the WAAM Ti-6Al-4V build, depicting large colony structures (~250 um in width) observed within the build (left) and along the build edge (right).

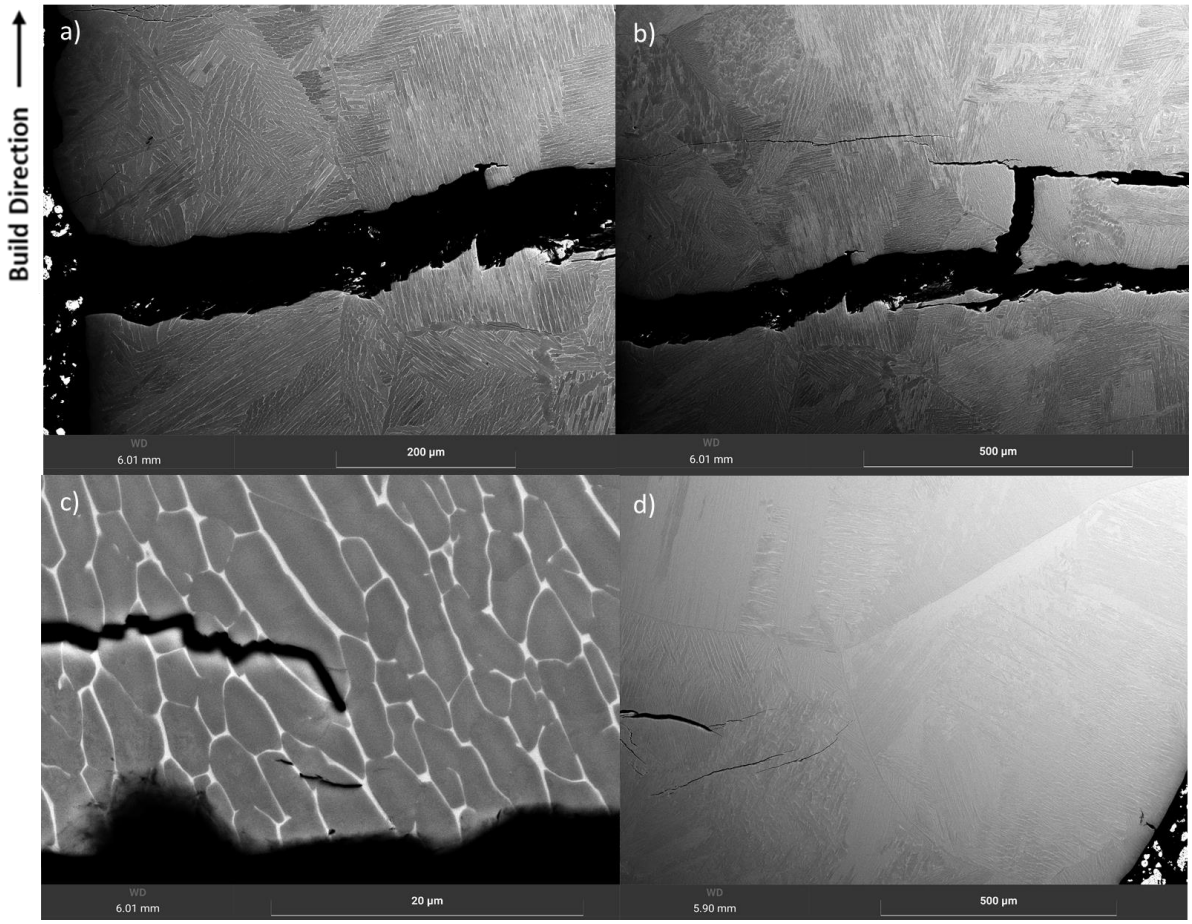

Figure 36A.4: Backscattter electron images of the crack propagation path at ~ 30 mm of the build height depicting a) the crack initiation site on the outer build surface and demonstrating no traversal of the prior β-Ti grain boundaries, b) continued propagation of the crack across colony structures and into two different crack paths, c) parallel and non-connecting crack propagation parallel to the main fracture, and d) the end of the crack path ~ 1 mm from the inner edge of the specimen width.

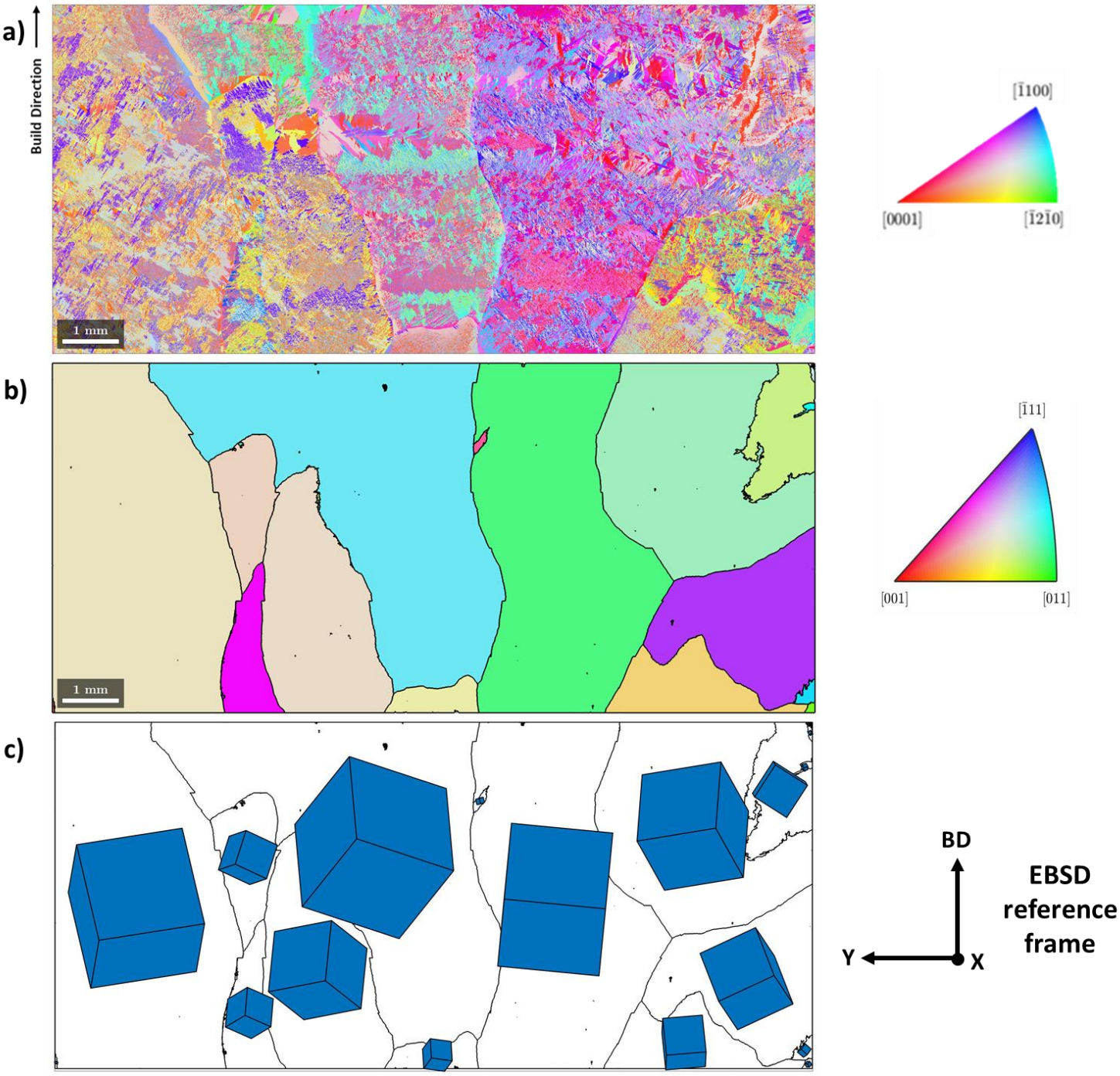

Figure 36A.5: Large-scale EBSD orientation maps for WAAM Ti-6Al-4V at ~ 15 mm in build height. α-Ti orientation EBSD (a) demonstrated a predominantly basketweave microstructure with clear Widmanstätten banding from each consecutive layer deposition. β-Ti reconstruction (b) of the as-solidified microstructure identifies the parent grain structure clearly observed in the α-Ti EBSD mapping. Overlaying the crystallographic orientation of each β-Ti grain was completed to more effectively demonstrate the solidification direction of the parent grains (c). All maps are colored with respect to the build direction.

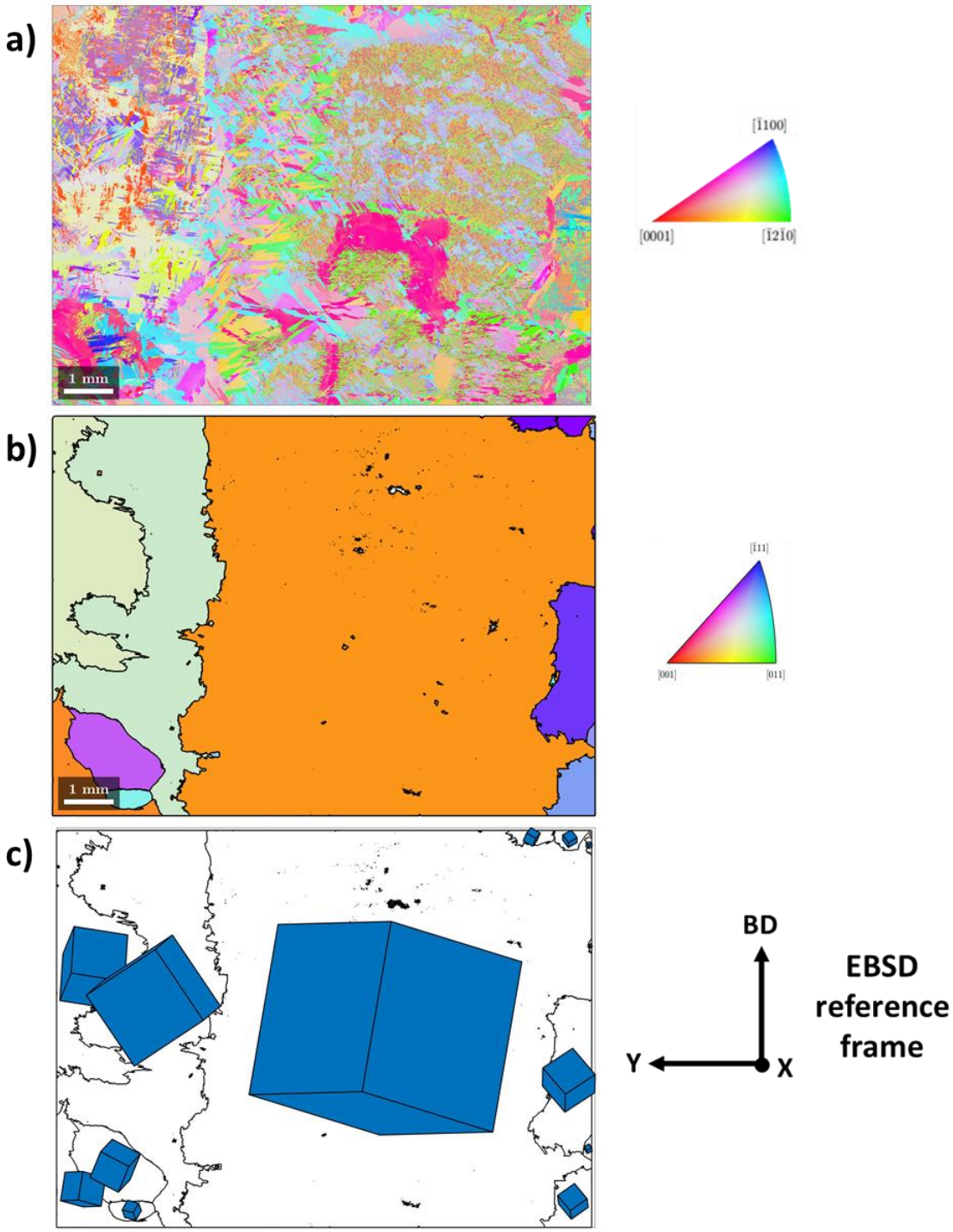

Figure 36A.6: Large-scale EBSD orientation maps for WAAM Ti-6Al-4V near the build finish and covering the effective width of the specimen. α-Ti orientation EBSD (a) again demonstrated a predominantly basketweave microstructure with Widmanstätten banding with each newly deposited layer. β-Ti reconstruction (b) revealed the majority of this specimen's width was made of one β-Ti grain during solidification and explains the highly textured α-Ti orientations observed here. Overlaying the crystallographic orientation of each β-Ti grain illustrates the largest parent grain exhibited a rotated cube texture along the build direction, again explaining the α-Ti orientations seen in EBSD and neutron diffraction. All maps are colored with respect to the build direction.

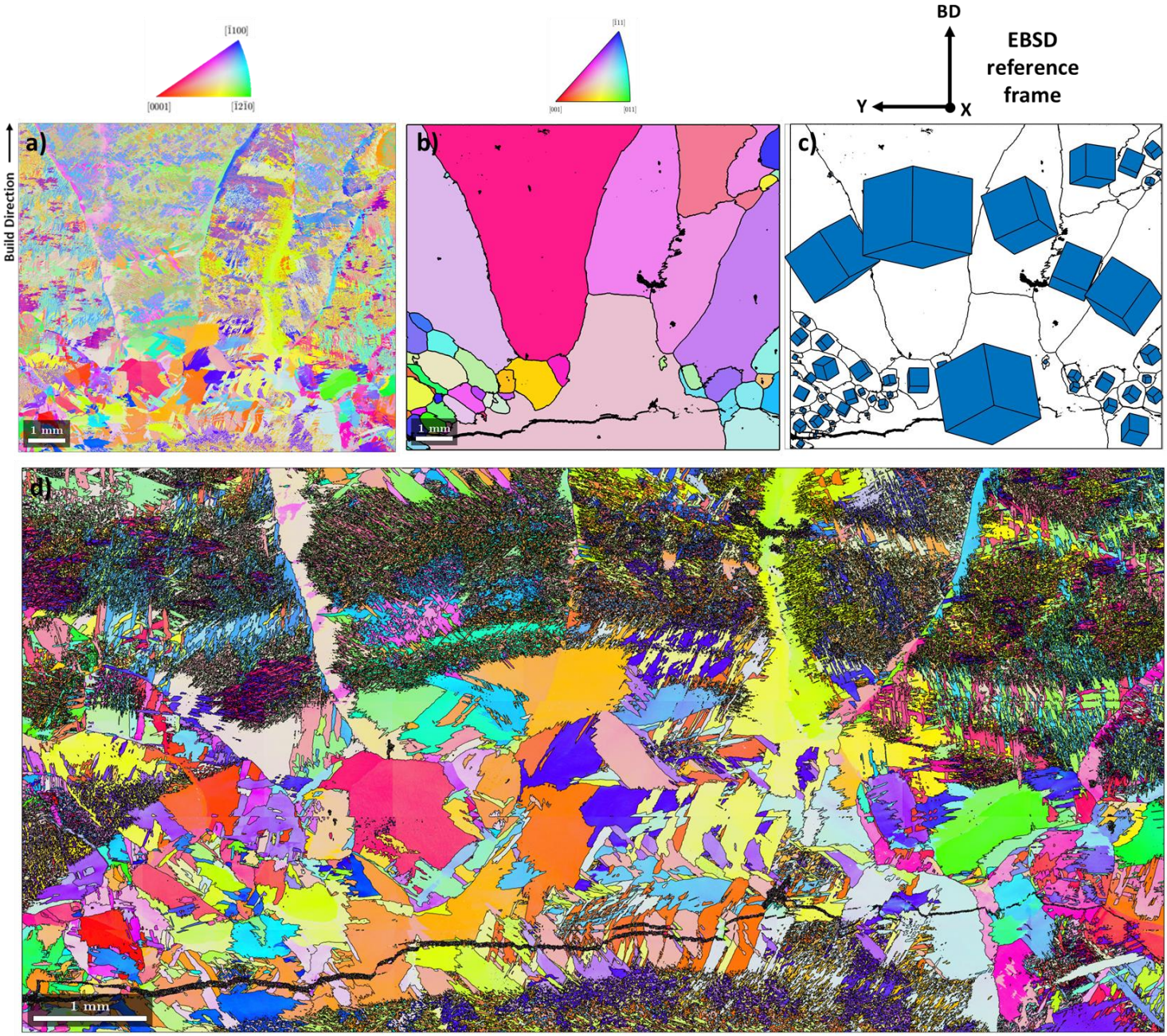

Figure 36A.7: Large-scale EBSD orientation maps for WAAM Ti-6Al-4V in a colony dominated region exhibiting significant cracking. α-Ti orientation mapping (a) demonstrated basketeave morphology in the top half of the surveyed area where large β-Ti grains can be observed with a colony microstructure towards the bottom portion. β-Ti reconstruction (b) demonstrated as-solidified grain geometries similar to a weld melt pool, bringing to light regions of equiaxed solidification and tilted columnar β-Ti grains. Overlaying crystal direction (c) demonstrates a clear directionality of the crystal structure to the grain growth direction, again reinforcing the theory this portion of material was subject to a lengthy pause and build restart. A finer EBSD survey of the cracked region (d) highlights the colony dominated region, and also outlines the crack propagation path more clearly. All maps colored with respect to the build direction.

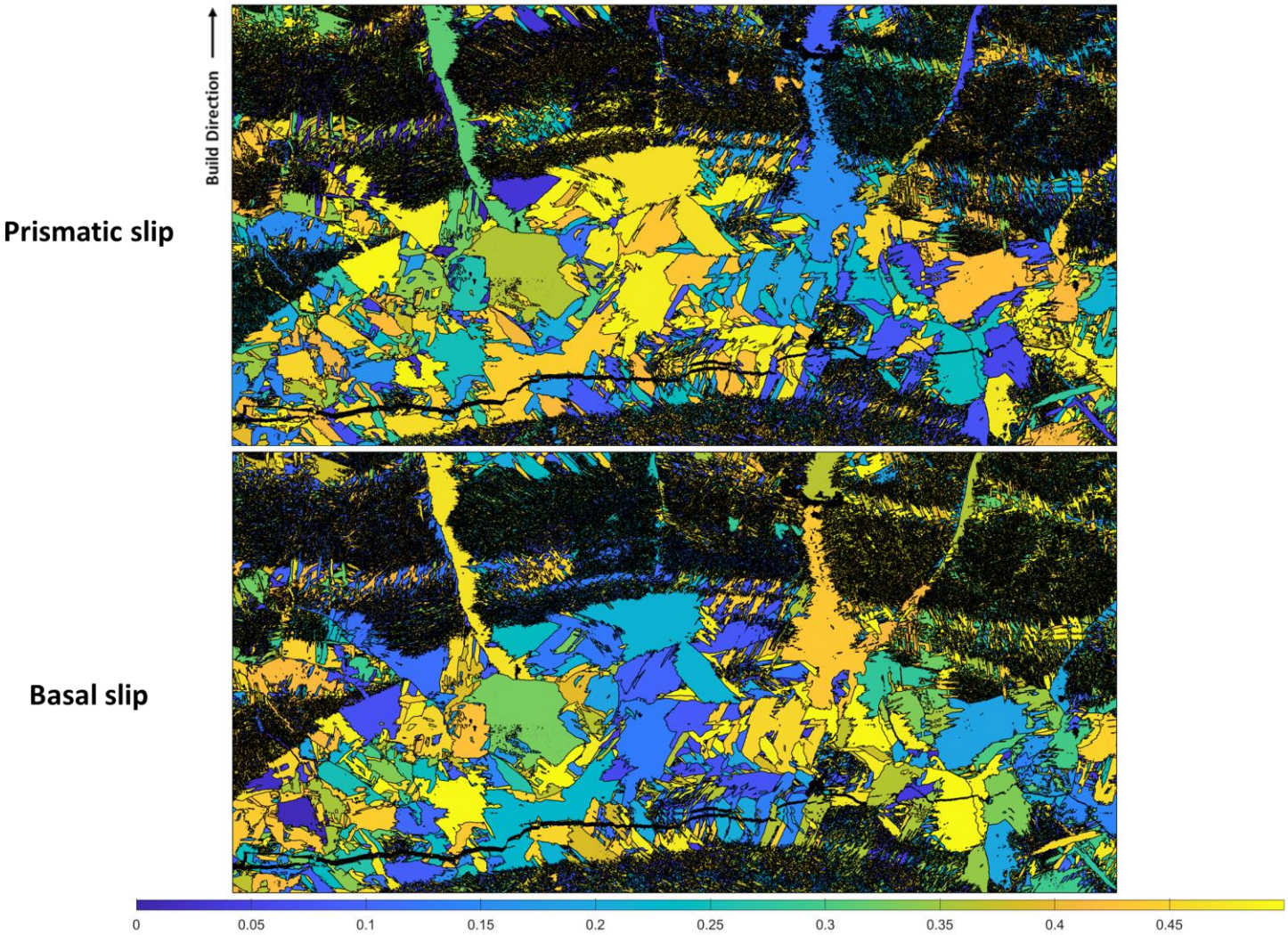

Figure 36A.8: Schmid factor maps of the cracked $\alpha + \beta$ colony region evaluated assuming a residual build stress aligned parallel to the build direction. The crack propagation in the colony microstructure was driven by whether prismatic and basal slip was more favorably aligned to the residual stress loading. Regions where neither slip system was preferentially aligned were found in some portions of the microstructure and corresponded to a more tortuous cracking path.

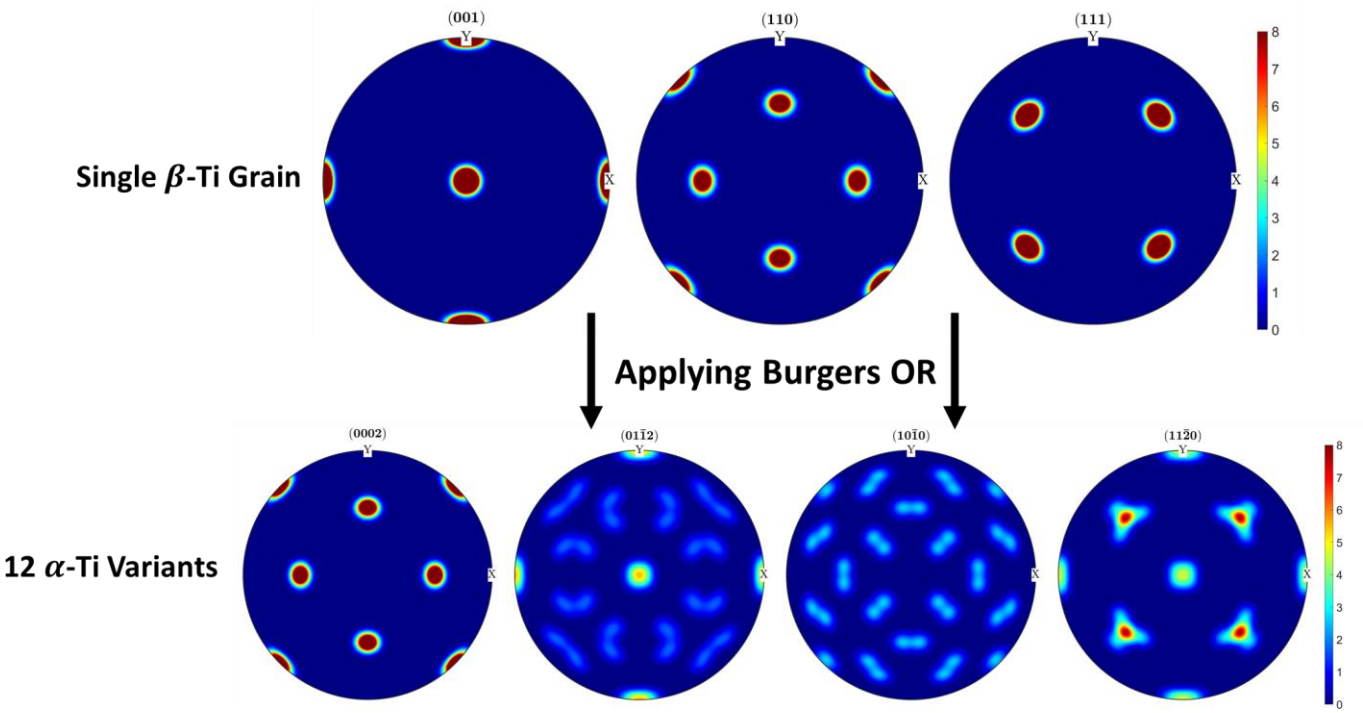

Figure 36A.9: Simulated $\beta \rightarrow \alpha$-Ti orientations using the Matlab plugin MTEX for a single, large β-Ti parent grain in pole figure. Assuming solidification out of the page, the single β-Ti parent grain (top) will transform to 12 α-Ti variants (bottom), 8 of which can be seen in the bottom set of pole figures. Due to the fixed location of the $\{110\}_{\beta}$ planes from the cubic solidification texture, no fiber texture can form like that seen in EBM-PBF Ti-6Al-4V. Thus, large β-Ti grains would reduce the likelihood of any such textures.

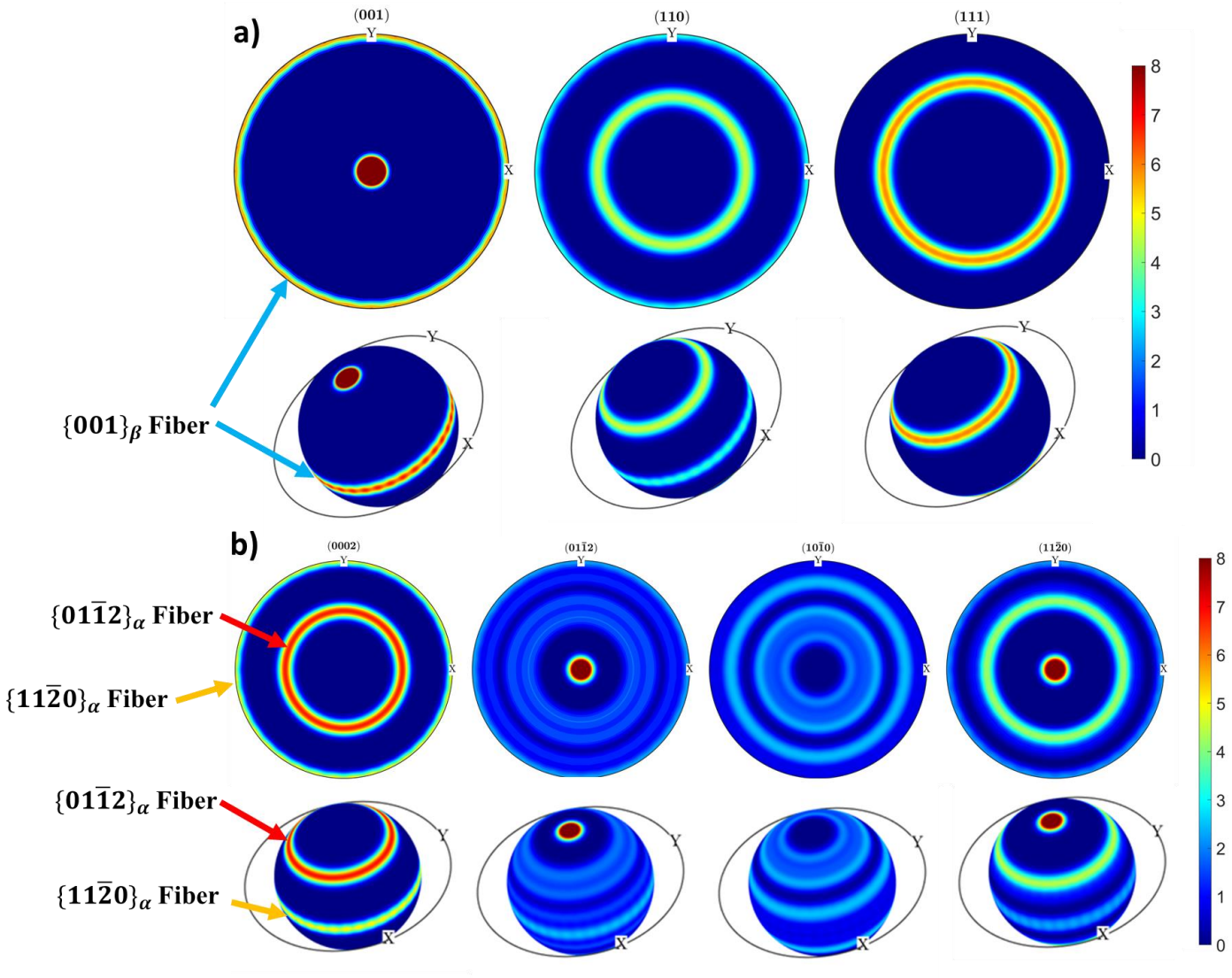

Figure 36A.10: Simulated $\beta \rightarrow \alpha$-Ti orientations using the Matlab plugin MTEX for 10 smaller β-Ti parent grains. **a)** 2D and 3D pole figures of multi-grain solidification of β-Ti. All 10 parent β-Ti grains have the same alignment of two $\{001\}_\beta$ planes along the solidification direction (out of the page). However, each β-Ti grain can freely rotate around this build direction. Assuming a random distribution of the four remaining $\{001\}_\beta$ around the two fixed $\{001\}_\beta$ planes, a ring of $\{110\}_\beta$ planes will be created on which α-Ti will form. **b)** 2D and 3D α-Ti pole figures, illustrating the product phase orientations resulting from 10 β-Ti grains oriented out of the page but free to rotate in-plane. The rings of $\{110\}_\beta$ planes mean α-Ti basal planes will form in a circular fashion around the solidification direction, producing the fiber textures seen in EBM-PBF Ti-6Al-4V [36A.6] and not significantly present in WAAM Ti-6Al-4V. Thus, fiber textures are a marker of how large the parent β-Ti grains are, while the type of α-Ti fiber texture determines the type of solid state microstructure present.

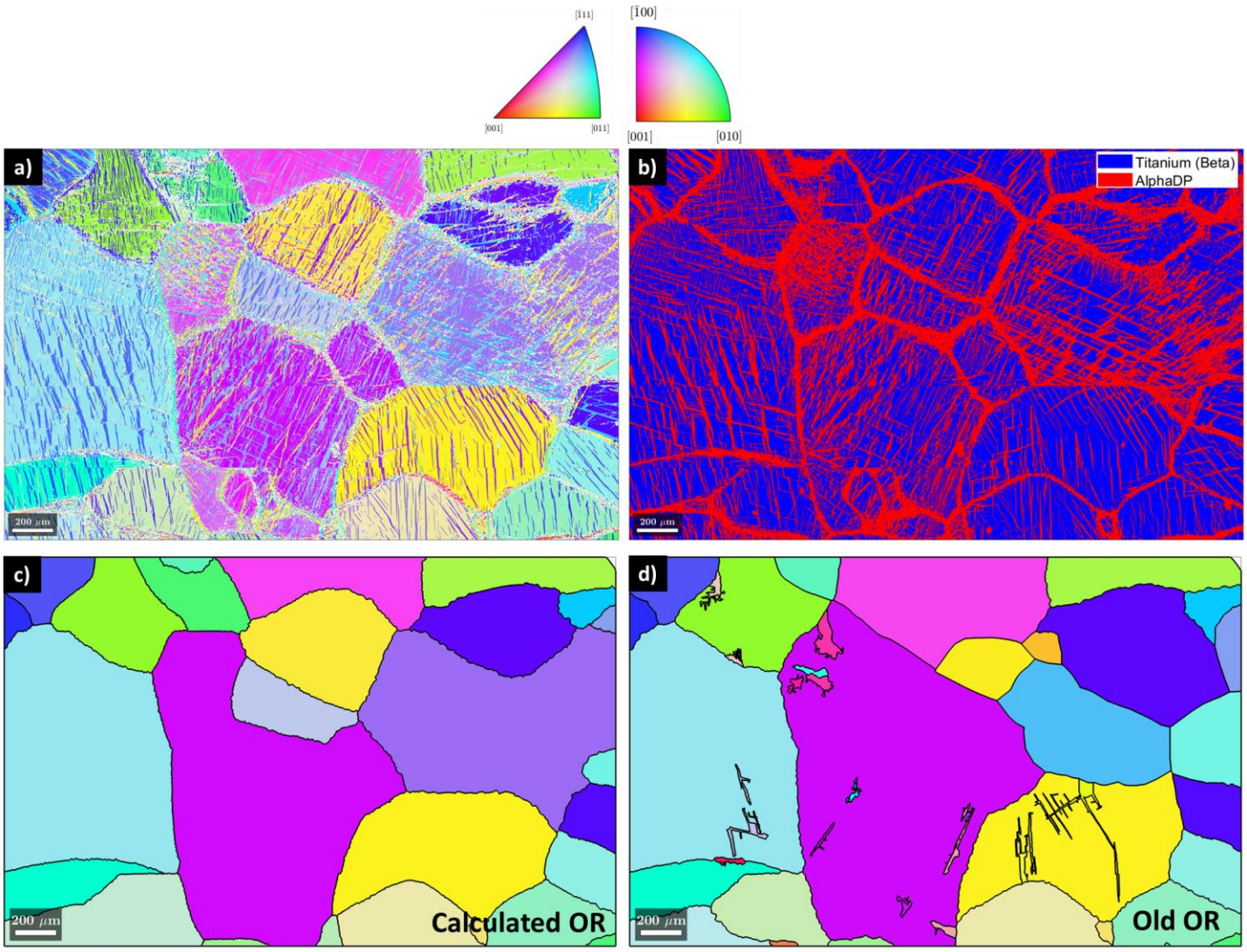

Figure 36A.11: **a)** Inverse pole figure (IPF) map of α'' and β-Ti Ti-10-2-3 microstructure after quenching from the β-Ti regime. Approximately 20% of the microstructure has transformed into α'' during quenching. **b)** Phase map of the orientation map illustrated in **(a)**. **c)** Reconstructed β-Ti IPF map using the MTEX calculated OR for the $\beta \rightarrow \alpha''$ transformation. Due to low misorientations between the adjoining purple β-Ti grains in the central area of the map, some parent grains were artificially merged together. Despite this, the calculated OR demonstrates an accurate match with the parent microstructure observed in **(a)**. **d)** Reconstructed β-Ti IPF map using the previously reported OR for Ti-10-2-3. A significant portion of the microstructure was incorrectly reconstructed, especially the right side of the orientation map. Further work is ongoing to identify how and why the calculated OR results in a better reconstruction than literature values and the limits to this applicability. All orientations are colored with respect to the normal direction (out of the page).

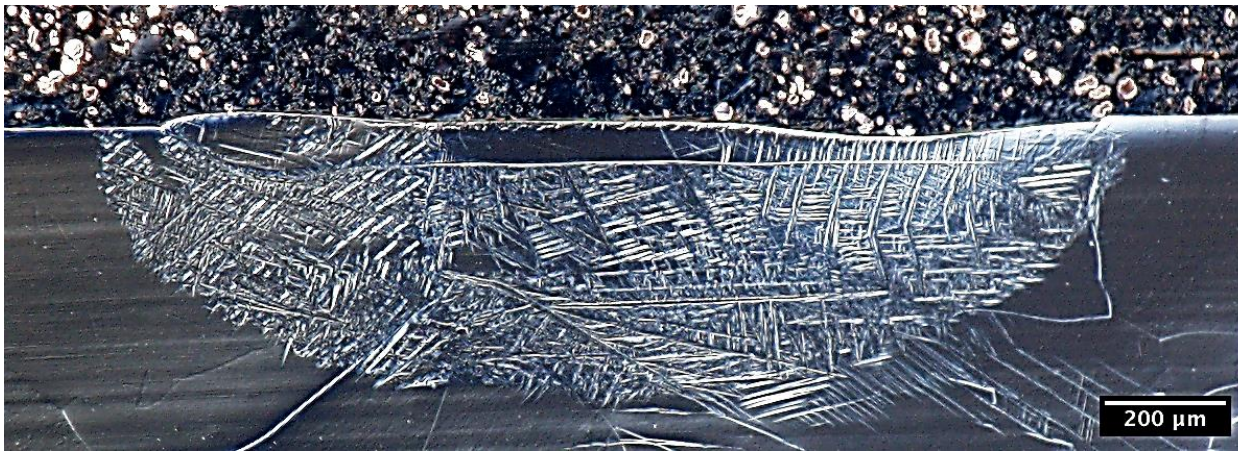

Figure 36A.12: Stress induced α'' in an etched Ti-10-2-3 AM sample melted at the Advanced Photon Source. Parent β-Ti grains are not obvious in the melt pool region and cannot be reliably inferred from the orientation of the martensite plates.